WATER RESOURCES RESEARCH, VOL. 36, NO. 11, PAGES 3337–3349, NOVEMBER 2000

Experiments on bar formation in a straight flume
1. Uniform sediment

Stefano Lanzoni

Dipartimento di Ingegneria Idraulica, Marittima e Geotecnica, Università di Padova, Padua, Italy

Abstract. Laboratory experiments have been carried out in a large laboratory flume using a nearly uniform sand and under controlled steady flow conditions such as to ensure the development of alternate bars on a ripple and/or dune-covered bed. The interaction between small-scale and large-scale bed forms is found to enhance a modulation in time and in space of the bar pattern. Moreover, the flow depth decrease experienced by the flow field when approaching bar fronts, leading to a progressive reduction of the dimensions of small-scale bed forms, may influence appreciably the overall flow resistance. Experimental values of bar wavelength and of bar celerity are compared with the theoretical estimates obtained from a model developed within the classical framework of linear stability analysis. In particular, the model accounts for the local variability of friction coefficient and water level, for the secondary helical flow effects, and for the influence of longitudinal slope on sediment transport. Quantitatively satisfactory predictions of bar wavelength appear to be possible in spite of the fact that in various runs a correct estimation of flow resistance and flow discharge appears to be relatively difficult.

1. Introduction

Under widely occurring circumstances, flow in a straight channel with erodible bed is unstable, and large-scale migrating bed forms develop. These bed forms, usually called alternate (free) bars, are characterized by a sequence of steep consecutive diagonal fronts with deep pools at the downstream face and gentler riffles along the upstream face. The changes in river morphology induced by the presence of such bed forms, whose height and wavelength scale with flow depth and channel width, respectively, have a nonnegligible impact on several aspects of river engineering such as the safe conveyance of water, sediment and ice, navigation, bank protection, the design of fluvial structures, water supply, fishery, and environmental protection.

In the last few decades a large number of studies, both theoretical and experimental, have been devoted to understanding the physical mechanisms underlying the formation and development of these bed forms and to predicting the conditions for their formation (see *Seminara and Tubino* [1989] and *Seminara* [1995] for an extensive review).

It is now fairly well understood that these processes can be explained in terms of an instability mechanism. The basic idea is that under appropriate conditions, the uniform flow taking place in a flat cohesionless bottom of a straight channel loses stability to infinitesimal three-dimensional (3-D) perturbations which consist of growing and migrating disturbances of length scale of channel width [*Hansen*, 1967; *Callander*, 1969; *Engelund and Skovgaard*, 1973; *Parker*, 1976; *Fredsoe*, 1978; *Blondeaux and Seminara*, 1985; *Colombini et al*., 1987; *Seminara and Tubino*, 1989]. Spatially growing steady disturbances can also arise forced by some nonuniform initial conditions [*Struiksma et al*., 1985; *Struiksma and Crosato*, 1989].

In linear stability analysis these perturbations are assumed to be small enough (strictly infinitesimal) for linearization to be a valid approximation. It is thus possible to determine the neutral stability conditions in the space of flow and sediment parameters. For the bar problem it turns out that in the plane given by the width to depth ratio β and the Shields parameter Θ, a neutral curve exists along which an infinitesimal disturbance neither grows nor decays. This curve exhibits a minimum value of β (critical conditions) above which bars are expected to grow. Within the context of a linear stability theory it is also possible to predict the wavelength and wave speed of the perturbations selected by the instability process (i.e., those corresponding to maximum growth rate), while, to the contrary, the bar amplitude remains undefined.

In order to estimate the equilibrium amplitude of a bar front, it is necessary to relax the linear constraint and account for the nonlinear interactions between different harmonics. Indeed, *Colombini et al*. [1987] showed that the weakly nonlinear interactions arising in a neighborhood of the minimum of the neutral marginal stability curve inhibit the indefinite growth predicted by the linear theory, the development of higher harmonics resulting in diagonal fronts with high downstream steepness. The wave speed of free alternate bars was also shown to be affected by nonlinearities.

As the width to depth ratio β increases, the strongly nonlinear competition between different modes not only affects significantly bar height and celerity but also enhances the selection of higher-mode configurations, namely, central bar mode or multiple row bar mode [*Colombini and Tubino*, 1991]. Moreover, because of the nonlinear interactions between perturbations of different wavelength, the periodic alternate bar pattern might become unstable under suitable values of the parameters and develop a modulation in time and in space, as shown by *Schielen et al*. [1993].

Existing experimental data [*Kinoshita*, 1961; *Ashida and Shiomi*, 1966; *Chang et al*., 1971; *Sukegawa*, 1971; *Muramoto and Fujita*, 1978; *Ikeda*, 1982; *Jaeggi*, 1984; *Fujita and Muramoto*, 1985; *Garcia and Niño*, 1993] seem to suggest that

Paper number 2000WR900160.
0043-1397/00/2000WR900160$09.00

despite that the above mathematical models are formally valid only within restricted ranges of parameters, a wider applicability is to be observed [see *Colombini et al*., 1987, Figure 7; *Garcia and Niño*, 1993, Figure 6]. Nevertheless, various questions still need to be investigated.

The criterion that the selected bar wavelength corresponds, for a given value of the width to depth ratio, to the maximum growth rate is not supported by any theoretical evidence except in a restricted neighborhood of the minimum of the neutral stability curve. Away from this minimum an increasingly large range of unstable wavelengths is excited, and although the growth rate always exhibits a maximum, it is an open question whether or not nonlinear interactions between different modes affect the development of bar wavelength. The weakly nonlinear models of *Colombini et al*. [1987] and *Schielen et al*. [1993] and the strongly nonlinear model of *Colombini and Tubino* [1991], in fact, are all concerned with the wavelength given by critical conditions. The experimental runs carried out by *Garcia and Niño* [1993] seem to indicate that the wavelength tends to increase from its critical value as β increases over the critical condition for the formation of alternate bars. Nevertheless, in the latter case a rapid tendency toward a constant value of the wavelength appears to occur. *Garcia and Niño* [1993] found that such a value tends to be underestimated by the wavelength corresponding to the critical condition. Moreover, the fully nonlinear computations carried out by *Nelson and Smith* [1989] suggest that nonlinear effects might be responsible for the lengthening of bar wavelength toward an equilibrium value experimentally observed by *Fujita and Muramoto* [1985].

Available experimental data are mostly concerned with a plane bed configuration. However, microscale (ripples) and macroscale (dunes) bed forms are likely to interact strongly with secondary flow induced by bars [*Tubino and Seminara*, 1990] and to affect bar formation itself. In addition, the above mentioned theoretical models assume either that the channel width is large enough or that the banks are not very steep, so that sidewall effects are negligible in the central region of the flow. This implies that experimental and theoretical results are comparable only for high values of the width to depth ratio. Hence, if the flume width is small (20–50 cm), the flow depth must be also small (1–4 cm) often implying that the Froude number of the flow is quite high (frequently greater than 1), while, usually, this is not the case in the prototype. Indeed, the transitional stage between the lower flow regime, characterized by a plane bed or by a dune-covered bed, and the upper flow regime, characterized by a plane bed or an antidune-covered bed, is generated for a Froude number of about 0.6–0.7 in flume conditions and of about 0.2–0.3 in field conditions [*van Rijn*, 1984].

The present contribution describes an extensive series of experiments carried out in a quite large flume under well-controlled steady flow conditions characterized by relatively moderate Froude numbers (i.e., small grain diameter to flow depth ratio) and by an initial bed configuration covered by ripples and/or dunes. The experimental results are then compared with the theoretical predictions obtained from a linear stability model which accounts for the variability of bottom friction coefficient, the secondary helical flow effects, and the influence of longitudinal slope on sediment transport. The paper is organized as follows. In section 2 the experimental apparatus is described along with data acquisition procedures and data processing. Section 3 is devoted to the discussion of the experimental results. The linear stability model and the comparison between experimental and theoretical results are described in section 4. Finally, section 5 reports some concluding remarks.

2. Materials, Experimental Apparatus, and Methods

2.1. Sediment

We report here on 11 experimental runs carried out with a single sediment. The sediment had a geometric mean diameter d_g^* of 0.48 mm, a d_{90}^* (i.e., the grain size for which 90% of the distribution is finer) of 0.71 mm, and a geometric standard deviation σ_g^* of 1.3 mm (here and in the following an asterisk will denote dimensional quantities). The grain size distribution was lognormal. Also, the sediment consisted almost entirely of quartz and nearly quartz density mineral, with a density $\rho_s = 2.65$ g/cm^3.

2.2. Experimental Apparatus

The experiments were made in a flume with a rectangular channel 55 m long, 1.5 m wide, and 1 m deep, with sidewalls consisting of a steel frame with glass windows. Water and sediment were recirculated separately. At the upstream end of the channel a 16 m long, 5 m wide stilling basin ensured a smooth and regular inflow into the flume. The water entering the stilling basin was supplied by a constant-level reservoir. At the downstream end of the flume the water passed over a V-shaped, 10.45 m long, 3.9 m wide sediment trap and fell over an automatically controlled tailgate. The water was then collected through a return flume to an underground water storage tank from which it was pumped to the constant-level reservoir. Water slope in the channel was established and/or maintained by adjusting the level of the tailgate. Water discharge was measured continuously through a Rehbock weir installed in the return flume.

The sediment trap located at the end of the flume caught virtually 100% of the passing sediment. The settling sediment was pumped continuously with a small discharge of water to a hydrocyclone installed at the upstream end of the flume. There water and sediment were separated, the sediment remaining in a small storage tank below the hydrocyclone. The increase in weight of this tank was continuously recorded by a balance system. When the increase in weight had reached a preset value, the storage tank automatically opened, and the sediment was dropped into the flume via a diffuser.

2.3. Methods

Two different kinds of experiments were carried out: the free bar tests and the forced bar tests. In free bar runs the initial bed configuration was almost plane, and the tailgate was initially adjusted to obtain the required energy slope while the water discharge was kept constant. Each experiment was stopped when equilibrium conditions were obtained, that is, when the bed slope was equal to water surface slope and, on average, the solid discharge and bar features reached nearly constant values. The forced bar experiments began immediately after the related free bar test; both water discharge and energy slope remained unchanged, but at the beginning of the channel, immediately after the sediment dropping section, a rectangular board of length B_{ob}^* was inserted next to the left sidewall, perpendicularly to the flow.

A summary of experimental conditions is reported in Table 1, where Q^* denotes water discharge, i_s is the water surface

Table 1. Summary of Hydraulic Experimental Conditions[a]

Run	Duration, hours	Q^*, L/s	i_s, %	D_0^*, cm	U_0^*, m/s	τ_0^{*I}, Pa	τ_0^*, Pa	Q_s^*, L/h
P1801	816	30	0.162	7.3	0.27	0.423	1.116	5.3
P2102[a]	720	30	0.162	7.3	0.27	0.423	1.116	5.3
P2403	260	47	0.205	8.3	0.38	0.720	1.587	30.1
P0404	192	40	0.201	7.7	0.35	0.631	1.451	25.4
P1204[b]	264	40	0.201	7.5	0.35	0.656	1.411	25.4
P2804[c]	360	40	0.201	7.5	0.35	0.656	1.411	25.4
P1505	28	30	0.452	4.4	0.45	1.167	1.884	94.5
P1605	24	20	0.495	3.3	0.40	1.011	1.558	71.8
P2709	24	45	0.514	5.7	0.53	1.497	2.764	225
P2809	24	40	0.517	5.3	0.50	1.405	2.592	194.3
P2909	24	45	0.516	5.6	0.53	1.530	2.734	215.4

[a] Definitions are as follows: Q^*, water discharge; i_s, water surface slope; D_0, average flow depth; U_0^*, average velocity; τ_0^{*I}, skin friction of the total bed shear stress τ_0^*; and Q_s^*, measured average volumetric solid discharge, including pores.
[b] This is a forced bar test with B_{ob}^* equal to 1/3 of the flume width.
[c] This is a forced bar test with B_{ob}^* equal to 2/3 of the flume width.

slope, D_0^* is the average flow depth, U_0^* is the average velocity, τ_0^{*I} is the skin friction portion of the total bed shear stress τ_0^*, and Q_s^* is the measured average volumetric solid discharge, including pores. Because of bed form presence, following *Wilcock* [1992], τ_0^{*I} was estimated using the drag-partition procedure of *Einstein* [1950] assuming $2d_{90}^*$ to be representative of grain roughness. The water surface slope and the average flow depth were evaluated from the measurements of the water level and of the bottom profile taken periodically within the flume. In particular, the bottom profile was measured at every centimeter along three different longitudinal sections by three profile indicators installed along the axis of the flume and 20 cm from each wall; simultaneously, a water level indicator located along the flume axis allowed measurement of water level. These instruments were mounted on a carriage, driven by a motor and riding on two rails parallel to the floor of the channel. The measuring reach of the flume ranged between 7.9 and 51.7 m. The upstream 7.9 m of the channel were not considered since a few channel widths were necessary to allow both the boundary layer to develop and the supplied sediment to spread within the entire cross section. The downstream limit of the measuring reach, moreover, was imposed by the overall size of the moving carriage.

3. Experimental Results

Before discussing in detail the experimental results, it may be worthwhile to briefly describe the evolution of bed topography observed in run P1801. In this run, in fact, owing to the low sediment transport rate, the final equilibrium state was reached very slowly. A few hours after starting the test, the initial flat bed configuration was altered by the presence of a nearly regular pattern of almost two-dimensional ripples with wavelength and height ranging between 15 and 30 cm and 0.5 and 1 cm, respectively. Later, some well-shaped bars began to appear, in particular, in the second half of the flume. The bars displayed wavelengths very close to the equilibrium values, while their amplitudes were very irregular and, on average, lower than the value characterizing the final configuration. Thus, as already observed by *Fujita and Muramoto* [1985], it appears that the bar height begins to grow quickly only after the bar wavelength, owing to bar edge formation, has almost reached its equilibrium value.

Figure 1 gives an overall view of the bottom configurations obtained at the end of each run. The final bed configuration observed in nearly all the runs was typical of a single row of alternating bars (see Figure 2a). However, in runs such as P1505 and P1605, characterized by relatively high values of the width to depth ratio (β being 17.0 and 22.7, respectively), although a central bar configuration never formed, the transverse profile exhibited a significant raising toward the axis, as shown in Figures 2b and 2c. The growth of small-scale bed forms such as ripples and/or dunes appeared to be a distinctive feature of all the experiments. Indeed, according to *van Rijn*'s [1984] classification of bed forms in the space given by the transport parameter T and the dimensionless particle size $\mathcal{D}_*$ the experimental points locate just on the boundary between the ripple and the dune regimes (i.e., $\mathcal{D}_* = 11.5$ and $T = 0.4–3.5$). A first consequence of the presence of small-scale bed forms was the difficulty of correctly estimating bar features. The longitudinal bottom profiles measured through the bottom profile indicators, in fact, were significantly distorted by high-frequency components. It was thus necessary to filter the detected signal using the moving average method [*Wang*, 1987]. A further piece of information was obtained from the analysis of the power spectrum of the recorded bed profiles.

The distinctive features of free bar are summarized in Table 2, where L_b^* denotes bar wavelength, H_b^* is bar height calculated as the difference between the maximum and the minimum bed elevation within a bar unit, and c_b^* is bar celerity estimated by comparing the plots of the longitudinal bed profiles after measurements taken at different times. It is worth noting that H_b^* generally underestimates the actual bar height since measurements of lateral bed profiles were taken 20 cm from the walls. The double value of the wavelength characterizing P2403, P0404, P1204, and P2804 is associated to the presence in the power spectra of the lateral profiles of two main peaks having comparable intensities and wavelengths differing by a factor of about 2 [*Lanzoni*, 1996]. A third minor peak was also detected displaying a wavelength similar to that associated with the predominant peak of the longitudinal axis profile, which, even in presence of bars, gives a reasonable estimate of ripple and/or dune wavelength [*Wang*, 1987].

The mutual interaction between bars and small-scale bed forms with wavelength and height ranging from 40 to 60 cm and from 2 to 4 cm, respectively, appeared to be extremely strong in runs P2304, P0404, P1204, and P2804. These runs where characterized by a remarkable time modulation in the bar pattern even after steady conditions were achieved. Periods

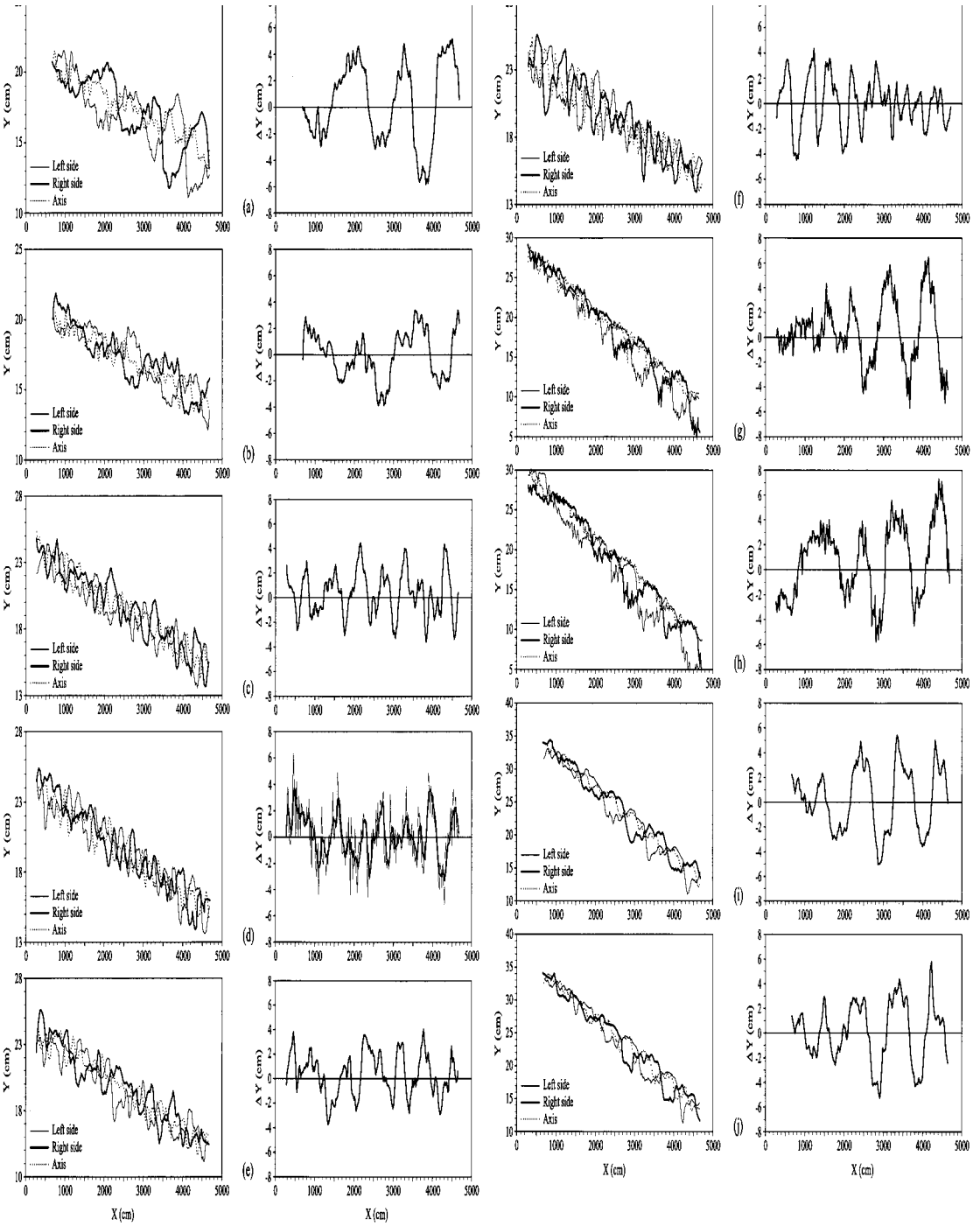

Figure 1. Examples of longitudinal bed profiles and difference between right side and left side bed elevation (ΔY) measured during the equilibrium phase of (a) P1801, (b) P2102, (c) P0404, (d) P1204, (e) P2804, (f) P2403, (g) P1505, (h) P1605, (i) P2809, and (j) P2909. The data are plotted every 20 cm and, excepting runs P1505 and P1605, are filtered by using a four points moving average procedure; in Figure 1d the raw data (thin curve) are also shown.

in which a rather regular train of bars was present in almost the entire flume were followed by intervals characterized by a very irregular bar topography. The existence of a spatial modulation of bar amplitude was less evident, even though Figure 1f suggests the possible presence of such a modulation. The relatively low number of bar wavelengths which can be contained within the measuring reach of the flume, in fact, makes it quite difficult to ascertain the presence of a spatial sequence of wave groups. Sometimes the fluctuations in bar features were caused by poorly developed bars which, from time to time, formed toward the upstream part of the flume. These partially formed bars, possibly triggered by random disturbances in the boundary conditions (i.e., water inflow and sand supply) and/or by the presence of smaller-scale bed forms, migrated downstream faster than the fully formed bars and were absorbed by the latter as soon as they superposed. This behavior resembles the

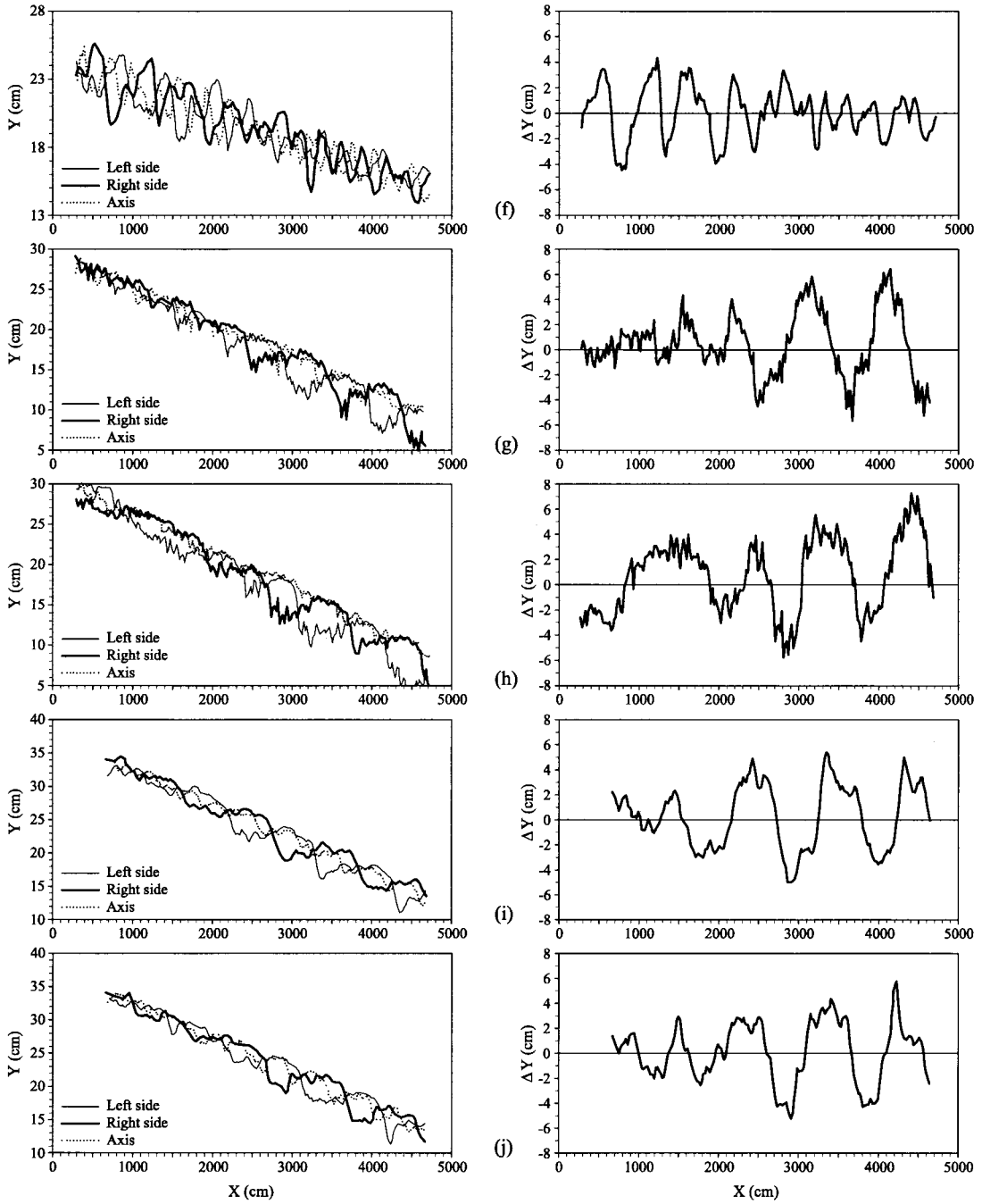

Figure 1. (continued)

theoretical picture outlined by *Schielen et al*. [1993] which showed that under suitable conditions, nonlinear interactions between perturbations of different wavelength might cause the periodic alternate bar pattern to become unstable, developing a modulation in time and in space. In particular, for a given value of the rate of change of the dimensionless sediment load function with respect to the Shields parameter (i.e., for the *Meyer-Peter and Müller* [1943] bed load formula, the quantity $2\Phi_T$ defined in Appendix A), a critical value of the friction coefficient C_0 exists below which the modulation arises. In present experiments, however, the values of C_0 (ranging from about 0.009 to 0.015) and of $2\Phi_T$ (ranging from about 3.7 to 9.8) fall outside the range theoretically predicted for the onset of modulation. Whether or not this occurrence is affected by the simplifying hypothesis embodied by *Schielen et al*.'s [1993] model (namely, constant Chezy coefficient, rigid lid approximation, and negligibility of both secondary helical flow and longitudinal bottom slope effects) still remains an open question.

Figure 3 shows the forced bar profile of P1202, P1204, and P2804 obtained by averaging over N independent sounds (N ranging between 19 and 29 for the different runs). Both a nondamped configuration (P1202) and a strongly damped configuration (P1204 and P2804) were observed, as can be inferred from Table 3. In both cases an extremely irregular sequence of free bars, usually strongly modulated, was observed to form

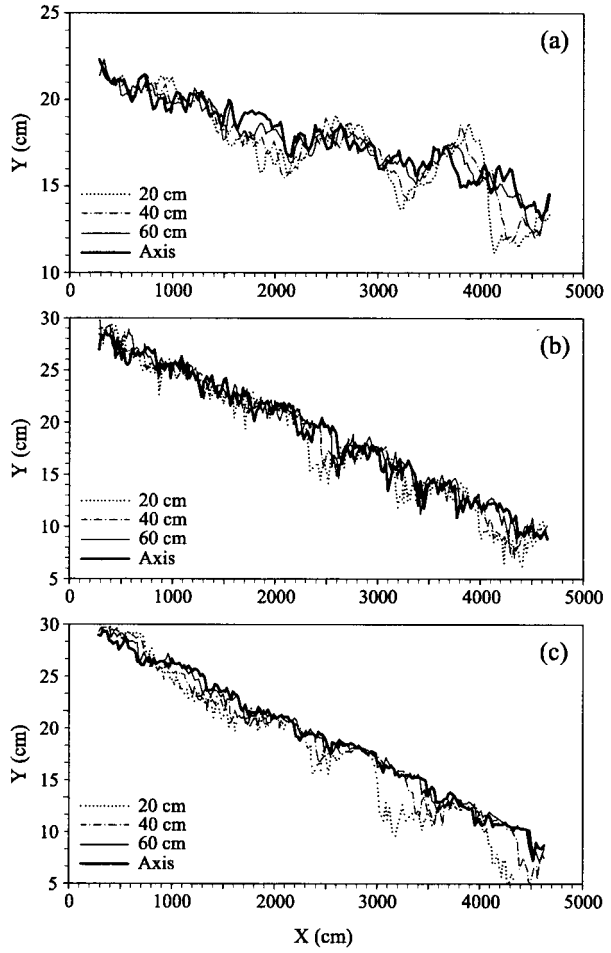

Figure 2. Additional longitudinal bed profiles measured at the end of (a) P1801, (b) P1505, and (c) P1605. The data, measured 20, 40, 60, and 75 cm from the left sidewall, are plotted every 20 cm and are filtered by using a four points moving average procedure.

toward the downstream end of the flume. A direct inspection of the longitudinal bed profile plots suggests that, especially in P2102, the amplitude of free bars was reduced, because of the presence of forced bars. This is in agreement with other stabilizing effects, induced by forced bars related to channel curvature, observed by *Kinoshita and Miwa* [1974] and explained theoretically by *Tubino and Seminara* [1990]. Regarding the ratio of forced to free bar wavelength, a reliable conclusion can hardly be attained, first, because of the long wavelength of the forced bar obtained in P2102 (i.e., about 2.5 times the wavelength of free bar) and, second, as a consequence of the strong damping displayed by P1204 and P2804 which makes it difficult to estimate correctly the forced bar wavelength.

The discussion of the experimental results has concentrated so far on the analysis of bar features; however, in view of the theoretical estimation of bar wavelength pursued in section 4, a brief discussion of the roughness and solid discharge predictors suitable to present experiments is timely here. Table 4 reports the comparison between the experimental values of the friction coefficient C_0 (corrected through *Einstein*'s [1950] procedure to account for sidewall effects) and the overall resistance coefficients estimated using various prediction methods. As mentioned above, the experiments fall just on the boundary between the ripple and the dune regimes. Indeed, the ripple regime formula elaborated by *Richardson and Simons* [1967] gives a quite satisfactory estimation of the friction coefficient in runs P1801, P2403, P0404, and P1204. The *Engelund and Hansen* [1967] partition method yield very similar results except for P1801 which, actually, appears to be more shifted than the others toward the ripple field ($\mathcal{D}_* = 11.5$ and $T = 0.4$). Finally, the *van Rijn* [1984] formula systematically predicts slightly lower values of the friction coefficient. The poor agreement between the observed and predicted data exhibited by runs P1505, P1605, P2709, P2809, and P2909 can be explained by the fact that, as a consequence of the relatively small average flow depth of these tests (in particular of P1505 and P1605), the dimensions of small-scale bed forms tend to decrease appreciably, especially when approaching bar fronts. Indeed, the values of the friction coefficients seem to indicate that an intermediate situation between the ripple and the plane bed regimes has been established in these runs. These data ultimately support the idea that even though the effect of flow separation taking place at bar front usually contributes weakly to flow resistance [*Parker*, 1978; *Bray*, 1979; *Jaeggi*, 1984], bars can indirectly influence flow resistance by the reduction (and/or amplification) of smaller-scale bed form dimensions through flow depth variations associated with the typical bar topography.

As far as sediment transport is concerned, the sediment appeared to be transported mainly as bed load. However, especially in runs characterized by higher values of the shear stress, it was observed that, from time to time, a certain amount of particles were put into suspension by the intermittent and intense vortices arising from the crests of smaller-scale bed forms. Figure 4 shows the comparison between observed values of Q_s^* and the sediment transport rates estimated using the *Engelund and Hansen* [1967] total load formula and the *Meyer-Peter and Müller* [1948] bed load formula. In the latter a dimensionless factor $\mu = \{\sqrt{C_0}\,(6 + 2.5 \ln [D_0^*/(0.9 d_{90}^*)]\}^{-3/2}$ has been introduced to account for the presence of ripples and/or small dunes on the bottom [*Vermeer*, 1986]. The agreement between measured and calculated sediment discharge appears to be fairly good except for P2709, P2809, and P2909 in which, actually, a certain amount of suspended load is likely to be expected because of the relatively high values of the bottom shear stress. Note that in the computations, the experimental value of the friction coefficient was adopted in order to obtain a better estimate of the effective solid discharge. Also,

Table 2. Free Bar Characteristics[a]

Run	L_b^*, m	H_b^*, cm	c_b^*, m/h
P1801	11.3	8.5	0.11
P2102[a]	11.6	4.0	···
P2403	4.5–7.5	5.0–6.0	0.8–0.9
P0404	4.3–8.0	6.0	0.70
P1204[b]	4.5–9.6	5.0	0.80
P2804[c]	8.0	5.0	0.75
P1505	10.0	7.0	2.80
P1605	11.0	7.7	···
P2709	9.7	4.5	5.80
P2809	10.6	4.7	5.10
P2909	9.5	4.4	5.00

[a] Definitions are as follows: L_b^*, bar wavelength; H_b^*, bar height; and c_b^*, bar celerity.
[b] This is a forced bar test with B_{ob}^* equal to 1/3 of the flume width.
[c] This is a forced bar test with B_{ob}^* equal to 2/3 of the flume.

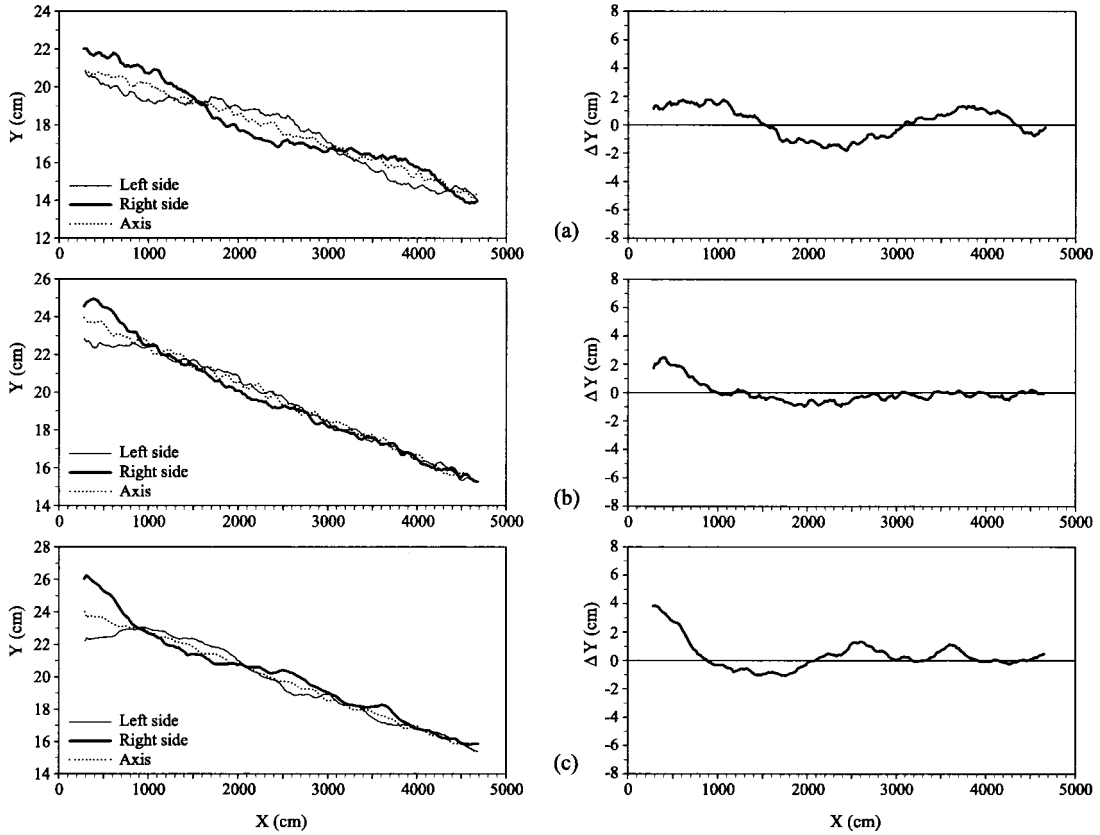

Figure 3. Forced bar longitudinal profiles and difference between right side and left side bed elevation (ΔY) calculated in (a) P2102, (b) P1204, and (c) P2804 by averaging over 19, 29, and 26 independent soundings, respectively. The data are plotted every 20 cm and are filtered by using a four points moving average procedure.

the adopted critical value of the Shields parameter (0.0311) has been derived following the procedure proposed by *van Rijn* [1984].

4. Mathematical Model

The linear stability analysis pursued in the present contribution follows closely the work of *Blondeaux and Seminara* [1985]. For the sake of completeness the analysis is here extended in order to account for (1) dispersive effects which arise in momentum equations as a consequence of performing the depth-averaging process, (2) secondary flow effects on the direction of the solid transport, and (3) influence of longitudinal bottom slope on sediment transport rate. These aspects of the phenomenon have already been considered, though not simultaneously, in other analytical models of bar formation in straight or meandering channels [*Struiksma and Crosato*, 1989; *Parker and Johannenson*, 1989]. However, at least to the knowledge of the author, it is the first time that they are included all together in a single model considering also the local variability of the friction coefficient and of the water level.

Table 3. Forced Bar Characteristics

Run	L_b^*, m	H_b^*I crest,[a] cm	H_b^*II crest,[a] cm
P2102[b]	30.0	1.6	1.3
P1204[b]	···	2.2	0.8
P2804[c]	···	3.8	1.0

[a] H_b^*I and H_b^*II denote the amplitude of the I and II front, respectively, of the forced bars which form within the flume.
[b] This is a forced bar test with B_{ob}^* equal to 1/3 of the flume width.
[c] This is a forced bar test with B_{ob}^* equal to 2/3 of the flume width.

4.1. Depth-Averaged Flow Field

Let us consider a straight alluvial channel with constant width $2B^*$ and nonerodible banks. The channel is assumed to

Table 4. Comparison Between the Measured Friction Coefficient C_0 and Various Theoretical Resistance Predictors[a]

Run	C_0	C_{RS}	C_{EH}	C_{vR}	C_{65}
P1801	0.0149	0.0120	0.0049	0.0058	0.0040
P2403	0.0111	0.0124	0.0125	0.0102	0.0038
P0404	0.0121	0.0126	0.0114	0.0093	0.0039
P1204[b]	0.0112	0.0127	0.0122	0.0098	0.0039
P1505	0.0091	0.0191	0.0194	0.0160	0.0047
P1605	0.0095	0.0213	0.0214	0.0169	0.0052
P2709	0.0100	0.0181	0.0177	0.0152	0.0043
P2809	0.0102	0.0186	0.0182	0.0154	0.0044
P2909	0.0096	0.0182	0.0178	0.0153	0.0043

[a] Theoretical resistance predictors are C_{EH} [*England and Hansen*, 1967], C_{vR} [*van Rijn*, 1984], C_{RS} [*Richardson and Simons*, 1967], and C_{90}, the plane bed skin friction coefficient (equal to $[6 + 2.5 \ln (D_0^*/2d_{90}^*)]^{-2}$).
[b] This is a forced bar test with B_{ob}^* equal to 1/3 of the flume width.

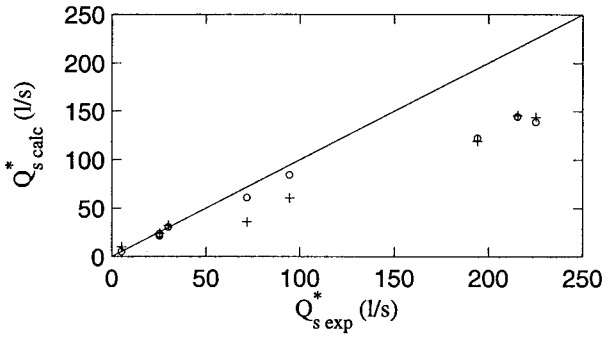

Figure 4. Comparison between experimental ($Q^*_{s\ \mathrm{exp}}$) and calculated ($Q^*_{s\ \mathrm{calc}}$) values of the solid discharge. Circles indicate *Meyer-Peter and Müller* [1948] bed load formula; plus signs indicate *Engelund and Hansen* [1967] total load formula. The perfect fit is represented by the solid line.

be wide enough for sidewall effects to be negligible in the central region. The bottom of the channel is made by cohesionless, nearly uniform sediment which is supposed to be transported mainly as bed load. The erodible bottom is assumed to vary slowly so that the quasi-steady flow field can be considered to adapt instantaneously to changes in bottom configuration.

To describe the flow problem, we refer to an orthogonal curvilinear coordinate system s^*, n^*, z^*, formed by the streamlines s^* and the normal lines n^* of the depth-averaged flow field and by the vertical axis z^*, positive in the upward direction. Denoting by D^*_0, U^*_0, and C_0, the constant flow depth, the average velocity, and the friction coefficient characterizing the uniform flow conditions (basic state), respectively, the variables of the problem are made dimensionless by using the following scaling:

$$(s^*, n^*) = B^*(s, n), \qquad (U^*, V^*) = U^*_0(U, V),$$
$$(\tau^*_s, \tau^*_n) = \rho U^{*2}_0(\tau_s, \tau_n), \tag{1}$$
$$(D^*, H^*) = D^*_0(D, HF^2_0), \qquad F_0 = U^*_0/\sqrt{(gD^*_0)},$$

where D is the local flow depth, H is the local water level above a given reference plane, U and V are the depth-averaged components on the local velocity, τ_s and τ_n are the components on the bed shear stress, F_0 is the uniform flow Froude number, and g is the gravity constant.

Since the channel considered here is a straight one, only the topographic deformations of the bottom due to bar growth affect, through streamline curvature, the flow field structure [*Parker and Johannenson*, 1989].

Moreover, the linear stability analysis developed in the following essentially applies to the early stages of bar growth. We thus assume the secondary flow to be a weak modification of the uniform basic flow field by introducing the following decomposition [*Kalkwijk and de Vriend*, 1980; *de Vriend*, 1981; *Parker and Johannenson*, 1989; *Seminara and Tubino*, 1992]:

$$u(s, n, z) = U(s, n)u_0(z) + O(\varepsilon^2), \tag{2}$$

$$v(s, n, z) = V(s, n)u_0(z) + \varepsilon v_{11}(s, n, z) + O(\varepsilon^2), \tag{3}$$

where ε is a small parameter (strictly infinitesimal), u and v are the local velocity components, v_{11} represents the effect of secondary helical flow driven by bottom topography on the transverse velocity v, and u_0 is the basic flow velocity profile which, modeling the Reynolds stresses through a parabolic eddy viscosity, obeys the classical logarithmic law [*Rozovskii*, 1957; *de Vriend*, 1981].

As a consequence of performing the depth-averaging process, two new dispersive terms of order ε arise on the right side of the classical de Saint Venant equations, which become

$$UU_{,s} + VU_{,n} + H_{,s} + \beta\frac{\tau_s}{D} = -\frac{\varepsilon}{D}(UD\overline{u_0v_{11}})_{,n}, \tag{4}$$

$$UV_{,s} + VV_{,n} + H_{,n} + \beta\frac{\tau_n}{D} = -\frac{\varepsilon}{D}(UD\overline{u_0v_{11}})_{,s}, \tag{5}$$

$$(DU)_{,s} + (DV)_{,n} = 0, \tag{6}$$

where an overbar denotes depth averaging, $\beta = B^*/D^*_0$, and the dimensionless components of bed shear stress τ_s and τ_n can be related to the depth-averaged velocity through the relationship

$$(\tau_s, \tau_n) = C(U, V)\sqrt{U^2 + V^2}. \tag{7}$$

The local friction coefficient C has to be specified through a suitable roughness predictor depending on the bed configuration considered. Furthermore, the dispersive terms appearing on the right side of (4) and (5), accounting for transverse diffusion of longitudinal momentum due to secondary flow, have to be related to the average flow characteristics by suitably modeling the secondary helical flow component v_{11}.

4.2. Secondary Helical Flow

On substituting decomposition (2) and (3) into the 3-D Reynolds flow equations, averaging over the vertical, and suitably combining the equations [see *Kalkwijk and de Vriend*, 1980; *de Vriend*, 1981], we obtain the following differential equation for the secondary flow component v_{11}

$$(u_0v_{11} - \overline{u_0v_{11}})_{,s} - \beta\sqrt{C_0}\,[(\nu_{\tau 0}v_{11,\zeta})_{,\zeta} + (\nu_{\tau 0}v_{11,\zeta})_{\zeta=\zeta 0}]$$
$$= -V_{,s}(u_0^2 - \overline{u_0^2}), \tag{8}$$

where $\nu_{\tau 0}$ is the unperturbed eddy viscosity and $\zeta = (z - \eta)/D$ is a stretched vertical coordinate whose lower limiting value ζ_0 is found by requiring that the depth-averaged value of u_0 be equal to 1.

The term on the right side of (8) represents the forcing due to streamline curvature induced by bottom topography. The first term on the left side of (8) accounts for the redistribution of secondary flow momentum by the streamwise convection. Neglecting this term allows us to obtain the secondary flow structure in fully developed flow conditions by simply assuming a self-similar structure of the velocity profiles, namely,

$$v_{11} = -\frac{V_{,s}}{\beta\sqrt{C_0}}\Gamma_0(\zeta), \tag{9}$$

where the form of the function $\Gamma_0(\zeta)$ depends on the profiles assumed for the velocity u_0 and the eddy viscosity $\nu_{\tau 0}$ [*de Vriend*, 1981].

Kalkwijk and Booij's [1986] numerical calculations have shown that there is quite satisfactory agreement between the analytical approximation (9) and the velocity profile calculated numerically by also retaining the first term on the left side of (8). This conclusion, however, does not apply to the bottom

shear stress since the secondary flow adapts faster to forcing term variations near the bottom than near the surface. Basically, we are interested in evaluating the modification of the sediment transport rate due to secondary helical flow; hence we need to also consider changes of secondary flow intensity in the streamwise direction. Thus a strict similarity hypothesis is no longer valid [*de Vriend*, 1981; *Olesen*, 1987], and the following generalization should be assumed

$$v_{11}(s, n, \zeta) = \frac{1}{\beta\sqrt{C_0}} I_0(s, n)\Gamma_0(s, \zeta), \tag{10}$$

where I_0 denotes the intensity of the secondary flow. However, the exact solution for I_0 and Γ_0 is hardly manageable analytically even within the context of a simple linear stability analysis. Here, following *Struiksma and Crosato* [1989], we assume that the effect of secondary flow convection can be neglected regarding the vertical distribution of v_{11} (i.e., Γ_0 does not depend on s), while the intensity of the secondary flow is evaluated from the equation obtained by substituting (10) into (8) and rearranging the various terms in the form

$$\lambda_r I_{0,s} + I_0 = -V_{,s}, \tag{11}$$

where the spiral motion adaptation length

$$\lambda_r = \frac{\Lambda_1}{\beta\sqrt{C_0}}$$

is evaluated on the basis of numerical studies [*Kalkwijk and de Vriend*, 1980; *de Vriend*, 1981; *Olesen*, 1987] to take into account empirically (through the dimensionless coefficient $\Lambda_1 \simeq 0.6$) the fact that the transverse bed shear stress adapts faster than the secondary helical flow intensity to changes in streamline curvature induced by variations of bed topography.

Moreover, recalling the decomposition (10), the dispersive terms on the right side of (4) and (5) can be expressed as

$$\overline{u_0 v_{11}} = \frac{\Lambda_2}{\beta\sqrt{C_0}} I_0 \qquad \Lambda_2 = \int_{\zeta 0}^{1} u_0\Gamma_0\, d\zeta,$$

where the coefficient Λ_2, which, in general, depends on grain size, is, on average, about 0.1 [*Kalkwijk and de Vriend*, 1980; *Tubino and Seminara*, 1990]. The expressions for Λ_1 and Λ_2 derived from the relationship proposed by *Kalkwijk and de Vriend* [1980] and *Kalkwijk and Booij* [1986] are reported in Appendix A.

4.3. Sediment Balance Equation

The dimensionless sediment balance equation reads as follows:

$$(F_0^2 H - D)_{,t} + Q_0(Q_{s,n} + Q_{n,n}) = 0, \tag{12}$$

with

$$(Q_s^*, Q_n^*) = (Q_s, Q_n)\sqrt{\Delta g d_g^{*3}}; \qquad Q_0 = \frac{\sqrt{\Delta g d_g^{*3}}}{(1-p) D_0^* U_0^*}$$

$$\Delta = \frac{\rho_s - \rho}{\rho}, \tag{13}$$

where Q_s and Q_n are the dimensionless components of sediment discharge, p is sediment porosity, and ρ_s and ρ are sediment and water densities, respectively.

Sediment transport is assumed to be determined by local flow conditions, its direction deviating from the direction of average bottom shear stress under the action of gravity because of transverse and longitudinal bed level slopes.

As demonstrated by *Seminara and Tubino* [1989], we can assume that at linear level, vectors and deviation angles in the plane locally tangent to the erodible bottom can be taken equal to their projection in the horizontal reference plane (s, n, z), namely,

$$(Q_s; Q_n) = (\cos\delta; \sin\delta)\Phi,$$

where Φ denotes the equilibrium sediment load function and δ is the angle between the sediment transport direction and the longitudinal s direction. It can be shown that the direction of sediment transport (i.e., of the average particle trajectories) can be written in the form [*Koch*, 1980]

$$\tan\delta = \frac{\sin\chi - \eta_{,n}/f(\Theta)}{\cos\chi - \eta_{,s}/f(\Theta)}, \tag{14}$$

where $\Theta = \tau^*/(\rho\Delta g d_g^*)$ is the dimensionless Shields parameter and $f(\Theta)$ is a weight function which, on the basis of bed leveling experiments [*Talmon et al.*, 1995], can be put in the form

$$f(\Theta) = 9(d_s/D)^{0.3}\Theta^{1.5}. \tag{15}$$

The angle χ between the direction of the bed shear stress and the direction of the channel axis is given by

$$\tan\chi = \tau_n/\tau_s \tag{16}$$

and is the sum of two contributions. The first is due to the deviation from straight uniform flow induced by bed topography; the second is connected to secondary flow. Substituting into (16) the decompositions (2) and (3) along with (10) yields

$$\tan\chi = \frac{V}{U} + \varepsilon\frac{I_0}{U\beta\sqrt{C_0}}\left[\frac{\Gamma_{0,\zeta}}{u_{0,\zeta}}\right]_{\zeta 0}, \tag{17}$$

where, assuming a parabolic eddy viscosity profile and, consequently, a logarithmic velocity distribution,

$$\left[\frac{\Gamma_{0,\zeta}}{u_{0,\zeta}}\right]_{\zeta 0} = -2\frac{\sqrt{C_0}}{k^2}\left(1 - \frac{\sqrt{C_0}}{k}\right),$$

k being the von Karman constant.

Finally, the effects of both helical flow and bed slopes on the magnitude of the sediment transport Φ can be accounted for by writing the usual Meyer-Peter and Müller bed load transport formula in the form [*Fernandez Luque and van Beek*, 1976; *Koch*, 1980]

$$\Phi = 8(\mu A\Theta - B\Theta_c)^{3/2}, \tag{18}$$

where

$$A = \cos(\delta - \chi) \simeq 1,$$

$$B = \frac{1}{\tan\varphi}\left(1 + \varepsilon\frac{\cos\chi}{\beta}\eta_{,s} + \varepsilon\frac{\sin\chi}{\beta}\eta_{,n}\right),$$

where φ is the critical drag angle of bottom sediment, μ is the ripple coefficient defined in section 3, and Θ_c is the critical value of the Shields parameter. Expanding (18) in terms of the small parameter ε yields

$$\Phi = 8\left(\mu\Theta - \frac{\Theta_c}{\tan\varphi}\right)^{3/2}(1 - \varepsilon\Lambda_3\eta_{,s} + O(\varepsilon^2)), \tag{19}$$

with

$$\Lambda_3 = \left[\frac{\Theta_c}{\mu \Theta \tan \varphi} \frac{\Theta}{\Phi} \Phi_{,\Theta} \right]_{\Theta_{0,1}}. \quad (20)$$

For transport formulas (as the Engelund-Hansen one) in which the solid discharge does not depend on critical shear stress, it is assumed that the transport rate is influenced by the slope through the relationship

$$\Phi = 0.05 \frac{\Theta^{5/2}}{C} (1 - \varepsilon \Lambda_3 \eta_{,s} + O(\varepsilon^2)). \quad (21)$$

4.4. Linear Stability Analysis

We consider basic flow perturbations of the form

$$(U, V, HF_0^2, D) = (1, 0, H_0 F_0^2, 1) + \varepsilon(U_1, V_1, H_1 F_0^2, D_1) + O(\varepsilon^2)$$

$$(Q_s, Q_n, \tau_s, \tau_n) = (Q_{s0}, 0, \tau_{s0}, 0) + \varepsilon(Q_{s1}, Q_{n1}, \tau_{s1}, \tau_{n1}) + O(\varepsilon^2).$$

On substituting these expansions into (4), (5), (6), (11), and (12) and performing linearization at order ε, we find

$$U_{1,s} + H_{1,s} + \beta C_0 [s_1 U_1 + (s_2 - 1) D_1] + \frac{\Lambda_2}{\beta \sqrt{C_0}} I_{0,n} = 0, \quad (22)$$

$$V_{1,s} + H_{1,n} + \beta C_0 \left[V_1 - \frac{2}{\beta k^2} \left(1 - \frac{\sqrt{C_0}}{k} \right) I_0 \right] + \frac{\Lambda_2}{\beta \sqrt{C_0}} I_{0,s} = 0, \quad (23)$$

$$U_{1,s} + V_{1,n} + D_{1,s} = 0, \quad (24)$$

$$\frac{\Lambda_1}{\beta \sqrt{C_0}} \lambda_r I_{0,s} + I_0 = -V_{1,s}, \quad (25)$$

$$\eta_{,t} + Q_0 \Phi_0 \left[f_1 U_{1,s} + f_2 D_{1,s} - \Lambda_3 \eta_{,ss} + V_{1,n} - \mathcal{R} \eta_{,nn} - \frac{2}{\beta k^2} \left(1 - \frac{\sqrt{C_0}}{k} \right) I_{0,n} \right] = 0, \quad (26)$$

where $\eta = F_0^2 H_1 - D_1$ and the various coefficients are given in Appendix A.

The linearity of the problem allows us to perform a normal mode analysis by considering perturbations of the form

$$(U_1, D_1, H_1) = (u_1, d_1, h_1) \sin(\pi m n/2) e^{\Omega t} e^{im(\alpha s - \omega t)} + \text{c.c.},$$

$$(V_1, I_0) = (v_1, \mathcal{I}_0) \cos(\pi m n/2) e^{\Omega t} e^{im(\alpha s - \omega t)} + \text{c.c.},$$

where α is the wavenumber, Ω and ω are the growth rate and the wave speed, respectively, of perturbations, i is the imaginary unit, $m = 1, 3, 5, \ldots$, and c.c. denotes the complex conjugate of a complex number. These decompositions, substituted into (22), (23), (24), and (26) after some algebra, lead to a dispersion relationship (extensively reported in Appendix A) of the form

$$\frac{\Omega - i\omega}{Q_0 \Phi_0} = \mathcal{F}(\alpha, \beta, d_s, \Theta_0, F_0^2, \Lambda_1, \Lambda_2, \Lambda_3), \quad (27)$$

with $\mathcal{F}$ being a complex function. For given values of the parameters F_0^2, d_s, Θ_0, Λ_1, Λ_2, and Λ_3 the dispersion relationship (27) allows one to determine the neutral conditions by requiring that the amplification factor Ω vanish. In the plane (α, β) this condition defines a marginal neutral stability curve which exhibits a minimum (critical conditions) at $\alpha = \alpha_c$ and $\beta = \beta_c$. For values of β lower than β_c, the uniform flow configuration analyzed is stable, and any small disturbance is damped out. For values of β greater than β_c a range of unstable wavelengths appears which enlarges with increasing β. The amplification rate, for a fixed value of β, exhibits a maximum which, within the context of a linear theory, is assumed to be representative of the wavelength selected by the instability mechanism. However, no theoretical evidence can substantiate this assumption: The strongly nonlinear interactions which are likely to arise when β and α do not fall within the neighborhood of the critical conditions prevent any conclusion in this sense.

In present calculations, on the basis of the experimental results discussed in section 3, the bed is assumed to be ripple covered (i.e., the *Richardson and Simons* [1967] roughness predictor has been adopted), while the *Meyer-Peter and Müller* [1948] bed load transport formula has been used to predict the sediment transport rate. Clearly, these assumptions turn out to be rather poor in the case of runs P1505, P1606, P2709, P2809, and P2909, partly because of the peculiar bed configuration exhibited by these runs and partly because of the fact that in runs P2709, P2809, and P2909 a certain amount of sediment is likely to be transported in suspension. Also, notice that there has not been any tuning of the parameters Λ_1, Λ_2, and Λ_3 whose adopted values were calculated according to the relationships reported in Appendix A and through (20).

Figure 5 shows the comparison between measured and calculated values of bar wavelengths. The agreement between observed and predicted wavelength appears to be satisfactory whenever the critical conditions are assumed to be representative of the selected wavelength (Figure 5a). However, the wavelength that, for the observed value of the width to depth ratio β, corresponds to the maximum growth rate $\Omega^*_{\max}$ systematically and significantly underestimates the actual bar wavelength (Figure 5b). These results support the idea that, as suggested by the quite slow bed evolution of P1801, the instability process first selects the wavelength (corresponding to the minimum of the stability curve) then enhances the growth rate of bar amplitude.

As discussed in section 3, because of the strong interaction between bars and smaller scale bed forms, the wavelengths distinctive of runs P2403, P0404, P1204, and P2804 are better represented by an interval (whose extremes are determined by the wavelengths corresponding to the first two peaks of the power spectrum) than a single point. In these runs the values of the critical wavelength appear to be very close to the maximum of the measured wavelength.

The introduction in the analysis of the effects related to the secondary helical flow and to the longitudinal bottom slope, in general, leads to an improvement of the estimated wavelength, as can be observed comparing Figures 5a and 5c. On average, the percentage errors between the experimental bar wavelength and the critical wavelength calculated by considering or neglecting the above effects are equal to 7.3 and 12.3, respectively, the maximum error being anyway less than 20% in both cases. These results seem to support the idea that although the production of helical flow due to streamline curvature may certainly have some influence on the selection of bar wavelength, yet it does not play the leading role as suggested by *Nelson and Smith* [1989].

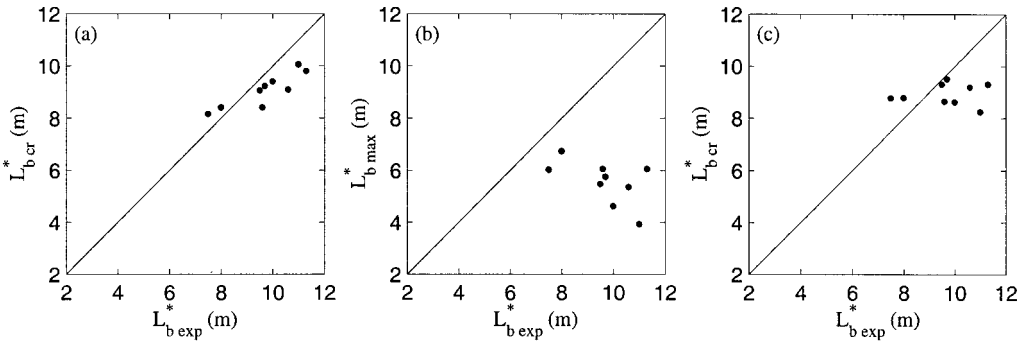

Figure 5. The wavelengths of alternate bars as predicted by the linear theory are compared with observed values of bar wavelengths $L^*_{b\,exp}$. (a) Critical wavelength $L^*_{b\,cr}$ calculated by including the effects of secondary helical flow and of longitudinal bottom slope (i.e., by estimating Λ_1, Λ_2, and Λ_3 through the relationship reported in Appendix A and through (20)); (b) Wavelength $L^*_{b\,max}$ that, given the experimental value of β, corresponds to the maximum growth rate, (c) Critical wavelength $L^*_{b\,cr}$ calculated by neglecting the effects of secondary helical flow and of longitudinal bottom slope (i.e., setting $\Lambda_1 = \Lambda_2 = \Lambda_3 = 0$). Notice that the latter case is equivalent to using *Blondeaux and Seminara*'s [1985] model.

Owing to the peculiar bed configuration exhibited by the equilibrium phase of P1505 and P1605, calculations have been performed also considering a plane roughness predictor jointly with the *Meyer-Peter and Müller* [1948] formula. The estimated wavelength, however, departed appreciably from the observed one. This can be explained by the fact that, as pointed out above, the wavelength is essentially controlled by the critical conditions, its value being scarcely influenced by the growth of bar height. Therefore it is the bed configuration typical of the earlier stages of bar growth (namely, the ripple-covered bed flat configuration) which has to be considered in the theoretical evaluation of the wavelength.

As far as the bar celerity is concerned, the scatter between computed and measured celerity values, shown in Figure 6, appears quite high. Indeed, as pointed out by *Colombini et al.* [1987], nonlinear interactions are likely to influence appreciably bar celerity. Also, we must recall that the computed bar celerity is directly proportional to the intensity of solid discharge whose computed values may depart appreciably from the observed ones.

A further notable feature of the linear solution is that theoretical results seem to explain the rather different trends exhibited by the forced bar profiles shown in Figure 3. The nearly no damping of forced bar amplitude characterizing run P2102 would suggest that in this run the width ratio β was definitively closer than in runs P1204 and P2804 to the threshold value β_r at which spatial perturbations neither grow nor decay. Within the context of the present theory, accounting for temporal modes rather than spatial modes, β_r simply coincides with the value of the width ratio for which temporally marginal stability conditions (i.e., $\Omega = 0$) and nonmigrating conditions (i.e., $\omega = 0$) are attained contemporaneously (e.g., the resonant mode of *Blondeaux and Seminara* [1985]). The values of β_r thus calculated suggest that runs P1204 and P2804 fall slightly below resonant conditions (which are $\beta = 10$ and $\beta_r \approx 10.5$). The perturbations arising in response to a finite disturbance of the initial conditions are then expected to damp in space, as experimentally observed. On the contrary, run P2102 is characterized by a value of β (10.3) well above the resonant value $\beta_r \approx 5.5$ thus implying, as explained by *Seminara and Tubino* [1992], the development in space of an equilibrium periodic configuration of steady bars. Theoretical results also reproduce, at least qualitatively, the tendency of run P2102 to select a wavelength of the forced bars longer than those observed in runs P1204 and P2804, the calculated wavelengths being equal to 42.8 and 36.2 m, respectively.

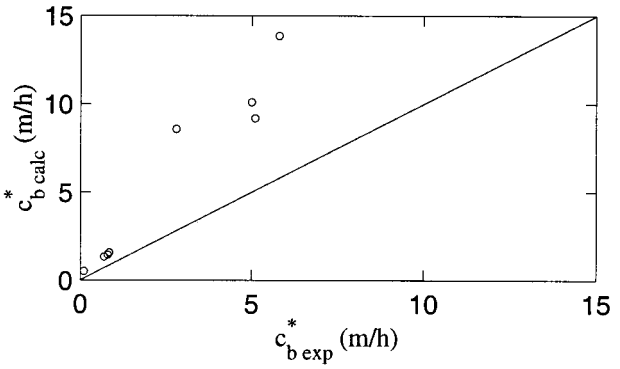

Figure 6. Comparison between observed ($c^*_{b\,exp}$) and calculated ($c^*_{b\,calc}$) values of bar celerity.

5. Conclusions

The results of a series of experiments carried out in a large laboratory flume aiming to elucidate various aspects of alternate bar development have been presented. Sediment grain size and flow characteristics were chosen to ensure the growth of both alternate bars and small-scale sand waves typical of the transition between the ripple and the dune regimes.

A first effect of the coexistence of large- and small-scale bed forms is to enrich the spectrum of bar wavelength with higher-frequency components. The mutual interaction between different bed forms, in fact, may induce the modulation in time and, likely, in space of bar characteristics observed in various experimental runs. Furthermore, depth variations associated with the typical alternate bar topography may lead to a reduction of ripple and dune dimensions which, in turn, produces a decrease of flow resistance with respect to the initial undisturbed bed configuration.

The theoretical values of bar wavelength and bar celerity obtained on the basis of a classical linear stability analysis

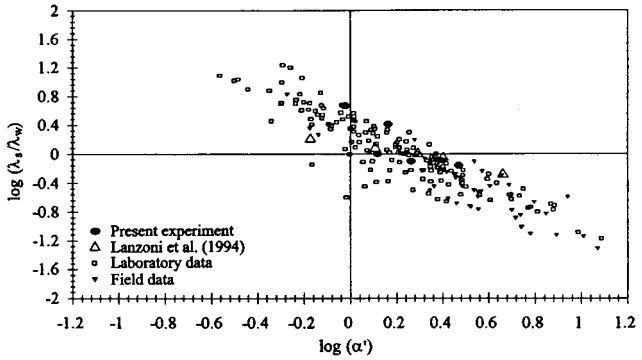

Figure 7. The observed interaction parameter λ_s/λ_w is plotted versus the modified wavenumber $\alpha' = \lambda_w\alpha$. Laboratory data are from *Ashida and Shiomi* [1966], *Jaeggi* [1984], *Kinoshita* [1961], *Muramoto and Fujita* [1978], *Sukegawa* [1971], and *Lanzoni et al*. [1994]. Field data are from *MacDonald* [1994].

appear to match the experimental data surprisingly well in spite of the fact that, owing to the particular bed configurations of certain runs (i.e., P1505, P1605, P2709, P2809, and P2909), suitable roughness and solid discharge predictors can be hardly specified. This circumstance appears even more unexpected if one considers the relatively high values assumed by the parameter $\varepsilon = (\beta - \beta_c)/\beta_c$ (ranging from 2 to 14) typical of present experiments, suggesting a nonnegligible influence of nonlinear interactions. Indeed, the values of ε prevent any comparison between observed bar heights and those predicted by the weakly nonlinear model of *Colombini et al*. [1987] (see Figure 6 of *Garcia and Niño* [1993]). However, as observed during the slow bottom evolution of P1801 and in accordance with *Fujita and Muramoto*'s [1985] experiments, it seems that bar wavelength is selected by the instability process soon after the bar front begins to grow, that is, in a neighborhood of critical conditions. Later the wavelength oscillates around the critical value, while the bar progressively achieves its equilibrium amplitude as a consequence of nonlinear interactions which inhibit the indefinite growth of perturbations predicted by the linear theory. Obviously, as found numerically by *Nelson and Smith* [1989], nonlinear effects (and, in particular, nonlinearity of convective acceleration) might also affect the equilibrium value of bar wavelength. Nevertheless, the dispersion relationship (27) still provides a quick and, at the same time, correct enough estimate of bar wavelength. Also, it allows an adequate explanation of the main features exhibited by spatially growing disturbances which may develop from nonuniform initial conditions.

The existence of a functional relationship relating bar wavelength to the parameters appearing in the dispersion relationship (27), moreover, is clearly suggested in Figure 7 where the available experimental data are rearranged on the basis of two suitable parameters which basically replace β and α. These parameters, whose importance was first recognized by *Struiksma et al*. [1985], are the interaction parameter λ_s/λ_w and a modified wavenumber $\alpha' = \lambda_w\alpha$, where $\lambda_w = 1/(2\beta C_0)$ and $\lambda_s = 4\beta f(\Theta)/\pi$ (with $f(\Theta)$ given by (15)) denote the flow and the bed adaptation lengths, respectively. Indeed, the experimental points, which include both laboratory and field data, show a quite sharp trend.

Some limitations of the present study will need further attention. In particular, nearly all experiments were characterized by predominant bed load transport except runs P2403, P2709, P2809, and P2909 which exhibited a certain amount of suspended load. The role played in bar formation and development by suspended sediment should be more deeply investigated both theoretically and experimentally. Finally, the role of the nonuniform character of sediment often exhibited by river beds is the subject of a companion paper [*Lanzoni*, this issue].

Appendix A

Coefficients of (22), (23), (24), (25), and (26) are as follows:

$$s_1 = \frac{2}{1 - C_T}, \qquad s_2 = \frac{C_D}{1 - C_T}, \tag{A1}$$

$$f_1 = \frac{2\Phi_T}{1 - C_T}, \qquad f_2 = \Phi_D \frac{C_D\Phi_T}{1 - C_T}, \tag{A2}$$

$$C_D = \frac{1}{C_0}\left[\frac{\partial C}{\partial D}\right]_{\Theta_0,1}, \qquad C_T = \frac{\Theta_0}{C_0}\left[\frac{\partial C}{\partial \Theta}\right]_{\Theta_0,1}, \tag{A3}$$

$$\Phi_D = \frac{1}{\Phi_0}\left[\frac{\partial \Phi}{\partial D}\right]_{\Theta_0,1}, \qquad \Phi_T = \frac{\Theta_0}{\Phi_0}\left[\frac{\partial \Phi}{\partial \Theta}\right]_{\Theta_0,1}. \tag{A4}$$

Dispersion relationship (27) is as follows:

$$\frac{\Omega - i\omega}{Q_0\Phi_0} = \frac{i\alpha}{\Psi - F_0^2}\left[\Psi(f_2 - f_1) + \frac{\pi^2}{4}\frac{1 - f_1}{i\alpha(a_{22} + \overline{a_{22}})} - \frac{\pi^2}{4}\frac{\mathcal{B}_1}{i\alpha(a_{22} + \overline{a_{22}})}\right] - \frac{\pi^2}{4}\mathcal{R} - \mathcal{B}_2, \tag{A5}$$

where

$$\Psi = \frac{1}{a_{11} - a_{14}}\left[i\alpha - \frac{a_{11}\pi^2/4}{i\alpha(a_{22} + \overline{a_{22}})} - \frac{\overline{a_{12}}\pi/2}{(a_{22} + \overline{a_{22}})}\right],$$

$$a_{11} = i\alpha + \beta C_0 s_1, \qquad a_{14} = \beta C_0(s_2 - 1), \qquad a_{22} = \beta C_0 + i\alpha,$$

$$\mathcal{B}_1 = -\frac{2}{\beta k^2}\left(1 - \frac{\sqrt{C_0}}{k}\right)\frac{i\alpha}{1 + i\alpha\lambda_r}, \qquad \mathcal{B}_2 = \frac{\Lambda_3}{\beta C_0}\alpha^2,$$

$$\mathcal{R} = \frac{1}{\beta f(\Theta_0)},$$

$$\overline{a_{12}} = \frac{\pi}{2}\frac{\Lambda_2}{\beta\sqrt{C_0}}\frac{i\alpha}{1 + i\alpha\lambda_r},$$

$$\overline{a_{22}} = -\left[i\alpha\frac{\Lambda_1}{\beta\sqrt{C_0}} - 2\frac{C_0}{k^2}\left(1 - \frac{\sqrt{C_0}}{k}\right)\right]\frac{i\alpha}{1 + i\alpha\lambda_r},$$

$$\Lambda_1 = \frac{1}{2k}\left(1 - 2\frac{\sqrt{C_0}}{k}\right),$$

$$\Lambda_2 = \sqrt{C_0}\left[5\frac{\sqrt{C_0}}{k} - 15.6\left(\frac{\sqrt{C_0}}{k}\right)^2 + 37.5\left(\frac{\sqrt{C_0}}{k}\right)^3\right]$$

It is worth noticing that the *Blondeaux and Seminara* [1985] eigenrelationship is immediately recovered by neglecting both secondary flow effects (i.e., imposing $\mathcal{B}_1 = \overline{a_{22}} = \overline{a_{12}} = 0$) and longitudinal bed slope effect (i.e., $\mathcal{B}_2 = 0$).

Acknowledgments. This research was carried out at the De Voorst River, Navigation and Structure Division of Delft Hydraulics within the context of EC Human Capital Mobility program. The author gratefully acknowledges N. Struiksma for the numerous fruitful discussions. The daily technical support ensured by J. Ouderling and F. de Groot was greatly appreciated.

References

Ashida, K., and Y. Shiomi, Study on the hydraulics behaviours of meander in channels, in *Disaster Prevention Research Institute Annuals*, *Rep. 9*, pp. 457–477, Kyoto Univ., Kyoto, Japan, 1966.

Blondeaux, P. and G. Seminara, A unified bar-bend theory of river meanders, *J. Fluid Mech*., *157*, 449–470, 1985.

Bray, D. I., Estimating average velocity in gravel bed rivers, *J. Hydraul. Div. Am. Soc. Civ. Eng*., *105*, 1103–1122, 1979.

Callander, R. A., Instability and river channels, *J. Fluid Mech*., *36*, 465–480, 1969.

Chang, H., D. B. Simons, and D. A. Woolhiser, Flume experiments on alternate bars formation, *J. Waterw. Harbors Coastal Eng. Div. Am. Soc. Civ. Eng*., *97*, 155–165, 1971.

Colombini, M., and M. Tubino, Finite-amplitude free bars: A fully nonlinear spectral solution, in *Sand Transport in Rivers*, *Estuaries and the Sea*, edited by R. Soulsby and R. Bettes, pp. 163–169, A. A. Balkema, Brookfield, Vt., 1991.

Colombini, M., G. Seminara, and M. Tubino, Finite-amplitude alternate bars, *J. Fluid Mech*., *181*, 213–232, 1987.

de Vriend, H. J., Steady flow in shallow channel bends, *Commun. Hydraul. 81-3*, Dep. of Civ. Eng., Delft Univ. of Technol., Delft, Netherlands, 1981.

Einstein, H. A., The bedload function for sediment transport in open channel flows, *Tech. Bull. 1026*, Soil Conserv. Serv., U.S. Dep. of Agric., Washington, D. C., Sept. 1950.

Engelund, F., and E. Hansen, *A Monograph on Sediment Transport in Alluvial Streams*, Danish Tech., Copenhagen, 1967.

Engelund, F., and O. Skovgaard, On the origin of meandering and braiding in alluvial streams, *J. Fluid Mech*., *57*, 289–302, 1973.

Fernandez Luque, F., R. van Beek, Erosion and transport of bed load sediment, *J. Hydraul. Res*., *14*, 127–144, 1976.

Fredsøe, J., Meandering and braiding of rivers, *J. Fluid Mech*., *84*, 609–624, 1978.

Fujita, Y., and Y. Muramoto, Studies on the process of development of alternate bars, *Bull. Disaster Prev. Res. Inst. Kyoto Univ*., *35*, (Part 3, *314*), pp. 55–86, 1985.

Garcia, M. H., and Y. Niño, Dynamics of sediment bars in straight and meandering channels: Experiments on the resonance phenomenon, *J. Hydraul. Res*., *31*, 739–761, 1993.

Hansen, E., On the formation of meanders as a stability problem, *Hydraul. Lab. Tech. Univ. Denmark Basic Res. Prog. Rep. 13*, pp. 9–13, Tech. Univ. of Denmark, Lyngby, 1967.

Ikeda, S., Prediction of alternate bar wavelength and height, *Rep. 12*, pp. 23–45, Dep. Found. Eng. and Const. Eng., Saitama Univ., Urawa, Japan, 1982.

Jaeggi, M., Formation and effects of alternate bars, *J. Hydraul. Eng*., *110*, 142–156, 1984.

Kalkwijk, J. P. T., and R. Booij, Adaptation of secondary flow in nearly-horizontal flow, *J. Hydraul. Res*., *24*, 19–37, 1986.

Kalkwijk, J. P. T., and H. J. de Vriend, Computation of the flow in shallow river bends, *J. Hydraul. Res*., *18*, 327–342, 1980.

Kinoshita, R., Investigation of channel deformation in Ishikari River, report, Dep. of Sci. and Technol., Bur. of Resour., Japan, 1961.

Kinoshita, R., and H. Miwa, River channel formation which prevents downstream translation of transverse bars (in Japanese), *Shinsabo*, *94*, 12–17, 1974.

Koch, F. G., Bed level computation for axisymmetric curved channels, *Rep. 657-IX*, Toegenpast Onderz. Waterstaat Rivers, Delft Hydraul., Delft, Netherlands, 1980.

Lanzoni, S., Experiments on free and forced bar formation in a straight flume, in *Uniform Sediment*, vol. I, *Res. Rep. Q1774*, Delft Hydraul., Delft, Netherlands, 1996.

Lanzoni, S., M. Tubino, and S. Bruno, Formazione di barre alternate in alvei incoerenti a granulometria non uniforme, paper presented at XXIII Convegno di Idraulica e Costruzioni Idrauliche, Idraul. e Cos.truz. Idraul., Naples, Italy, settembre, 20–25, 1994.

Meyer-Peter, E., R. Müller, Formulas for bedload transport, paper presented at 2nd Congress IAHR, Int. Assoc. of Hydraul. Res., Sweden, Stockholm, 1948.

MacDonald, M., Restoration and improvement of the Marala-Ravi Link System, internal report, 27 pp., Delft Hydraul., Delft, Netherlands, 1994.

Muramoto, Y., and Y. Fujita, The classification of meso-scale river bed configuration and the criterion of its formation, paper presented at 22nd Japanese Conference on Hydraulics, Jpn. Soc. Civ. Eng., 1978.

Nelson, J. M., and D. J. Smith, Evolution and stability of erodible channel beds, in *River Meandering*, *Water Resour. Monogr*., vol. 12, edited by S. Ikeda and G. Parker, pp. 321–377, AGU, Washington, D. C., 1989.

Olesen, K. W., Bed topography in shallow river bends, *Commun. Hydraul. Geotech. Eng. 87-1*, Delft Univ. of Technol., Delft, Netherlands, 1987.

Parker, G., On the cause and characteristic scales of meandering and braiding in rivers, *J. Fluid Mech*., *76*, 457–480, 1976.

Parker, G., Self-formed straight rivers with equilibrium banks and mobile bed, 2, The gravel river, *J. Fluid Mech*., *89*, 127–147, 1978.

Parker, G., and H. Johannenson, Observations on recent theories of resonance and overdeepening in meandering channels, in *River Meandering*, *Water Resour. Monogr*., vol. 12, edited by S. Ikeda and G. Parker, pp. 379–415, AGU, Washington, D. C., 1989.

Richardson, E. V., and D. B. Simons, Resistence to flow in sand channels, paper presented at 12th Congress IAHR, Int. Assoc. of Hydraul. Res., Fort Collins, Color., 1967.

Rozovskii, I. L., Flow of water in bends of open channels (in Russian), report, Acad. of Sci. of Ukr. Sov. Soc Repub., 1957. (English translation available as *OTS* 60-51133 from Off. Tech. Serv., U.S. Dep. of Commer. Washington, D. C., 1961)

Schielen, R., A. Doelman, and H. E. de Swart, On the nonlinear dynamics of free bars in straight channels, *J. Fluid Mech*., *252*, 325–356, 1993.

Seminara, G., Effect of grain sorting on the formation of bedforms, in *Sediment Transport Mechanisms in Coastal Environments and Rivers*, edited by R. D. Rajaona, *Appl. Mech. Rev*., *48*, 549–563, 1995.

Seminara, G., and M. Tubino, Alternate bars and meandering: Free, forced and mixed interactions, in *River Meandering*, *Water Resour. Monogr*., vol. 12, edited by S. Ikeda and G. Parker, pp. 267–320, AGU, Washington, D. C., 1989.

Seminara, G., and M. Tubino, Weakly nonlinear theory of regular meanders, *J. Fluid Mech*., *224*, 257–288, 1992.

Struiksma, N., and A. Crosato, Analysis of a 2-D bed topography model for rivers, in *River Meandering*, *Water Resour. Monogr*., vol. 12, edited by S. Ikeda and G. Parker, pp. 153–180, AGU, Washington, D. C., 1989.

Struiksma, N., K. W. Olesen, C. Flokstra, and H. J. de Vriend, Bed deformation in curved alluvial channels, *J. Hydraul. Res*., *23*, 57–79, 1985.

Sukegawa, N., Study on meandering of streams in straight channels, report Dep. Sci. and Technol., Bur. of Resour., Japan, 1971.

Talmon, A. M., M. C. L. M. van Mierlo, and N. Struiksma, Laboratory measurements of the direction of sediment transport on transverse alluvial-bed slopes, *J. Hydraul. Res*., *33*, 495–517, 1995.

Tubino, M., and G. Seminara, Free-forced interactions in developing meanders and suppression of free bars, *J. Fluid Mech*., *214*, 131–159, 1990.

Vermeer, K., The ripple factor in sediment transport equations, *Rep. R657/M1314-V*, Toegenpast Onderz. Waterstaat Rivers, Delft Hydraul., Delft, Netherlands, 1986.

van Rijn, L. C., Sediment transport, III, Bedforms and alluvial roughness, *J. Hydraul. Eng*., *110*, 1733–1754, 1984.

Wang, D. G., Three-dimensional phenomena in straight flumes, *Rep. R657-XXVIII*, *R1625*, Toegenpast Onderz. Waterstaat Rivers, Delft Hydraul., Delft, Netherlands, 1987.

Wilcock, P. R., Experimental investigation on the effect of mixture properties on transport dynamics, in *Dynamics of Gravel-Bed Rivers*, edited by P. Billi et al., pp. 109–139, John Wiley, New York, 1992.

S. Lanzoni, Dipartimento di Ingegneria Idraulica, Marittima e Geotecnica, Università di Padova, via Loredan 20, I-35131 Padua, Italy. (lanzo@idra.unipd.it)

(Received February 23, 1999; revised May 15, 2000;
accepted May 17, 2000.)